The International Journal of Advanced Manufacturing Technology (2022) 121:3685–3701
https://doi.org/10.1007/s00170-022-09503-7

ORIGINAL ARTICLE

Residual oxygen content and powder recycling: effects on microstructure and mechanical properties of additively manufactured Ti-6Al-4V parts

Nicole Emminghaus[1] · Robert Bernhard[1] · Jörg Hermsdorf[1] · Stefan Kaierle[1,2]

Received: 3 January 2022 / Accepted: 1 June 2022 / Published online: 24 June 2022

Abstract
The laser-based powder bed fusion of metals (PBF-LB/M) offers a variety of advantages over conventional processing techniques and the possibility to recycle and reuse powder increases its sustainability. However, the process and resulting part properties are influenced by a variety of factors including powder recycling grade and residual oxygen content of the process atmosphere. Especially in terms of reactive materials like Ti-6Al-4V, oxidation during processing and recycling determines process stability and reproducibility. This work therefore focusses on the influence of the conventionally varied processing parameters as well as atmosphere residual oxygen content process and powder recycling on the microstructure and mechanical properties. For this purpose, the design of experiments approach is used and by evaluation of regression models, effect sizes and interactions are given. Additionally, two different etching techniques were employed to reveal different aspects of the microstructure. While no significant influence of powder recycling and residual oxygen on the microstructure could be observed, they both significantly influence the mechanical properties. A maximum hardness of 470 HV0.1, a maximum ultimate tensile strength of 1252.3 MPa, and a maximum elongation at break of 17.8 % were obtained. The results demonstrate the importance of the processing atmosphere's residual oxygen content and of taking into account the changing powder characteristics during recycling as well as its effect on the part properties.

Keywords Additive manufacturing · Laser-based powder bed fusion · Ti-6Al-4V · Design of experiments · Mechanical properties · Microstructure

1 Introduction

The additive manufacturing (AM) technique laser-based powder bed fusion of metals (PBF-LB/M according to DIN EN ISO/ASTM 52900, formerly known as selective laser melting) experienced increasing interest over the last years due to the ability of manufacturing net-shaped metal parts with intricate geometries directly from CAD (computer-aided design) models [1–3]. This is especially advantageous for lightweight parts in the aerospace industry [4, 5] or patient-specific individual implants [6, 7]. For these applications, also the most frequently used titanium alloy Ti-6Al-4V (Ti – 6 wt% Al – 4 wt% V) is of particular interest owing to its high specific strength, low density, biocompatibility, and corrosion resistance [8, 9]. Due to the high cooling rates of 10^3–10^8 K/s present in the PBF-LB process [10–12], this α+β alloy forms a non-equilibrium, fine martensitic microstructure in the as-built condition. Thereby, the α/α'-laths are formed in prior β-grains. The cooling rate and thus the microstructure depend on the volume energy density E_V (Eq. 1) applied in the process.

$$E_V = \frac{P}{v \cdot h \cdot t} \tag{1}$$

The volume energy density is a frequently used metric in parameter studies in PBF-LB [14–17] and contains the main processing parameters laser power P, scanning speed v, hatch spacing h, and layer thickness t. Nevertheless, the single underlying parameters and their interaction effects

✉ Nicole Emminghaus
n.emminghaus@lzh.de

[1] Laser Zentrum Hannover e.V. (LZH), Hollerithallee 8, Hannover D-30419, Germany

[2] Leibniz Universität Hannover, Institut für Transport- und Automatisierungstechnik (ITA), An der Universität 2, Garbsen D-30823, Germany

need to be understood since they affect the melt pool and therefore the resulting microstructure in various ways. Additionally, as a prerequisite for the formation of martensite, the martensite start temperature (M_S) needs to be lower than the build temperature. It depends on the initial microstructure, chemical composition, and composition homogeneity as well as on the presence of impurity elements [18, 19]. Therefore, the type of powder and its recycling grade as well as the oxygen content present in the process atmosphere are also likely to have an impact on the resulting microstructure. In various studies, it could be shown that powder recycling leads to changes in powder properties. These are caused by heat influences and oxidation during processing leading to a changed chemical composition, as well as spattering and sintering resulting in larger particles [20–24]. For example, an increased oxygen content could be seen in recycled powder [25–28]. Moreover, Carrion et al. investigated the effect of powder reuse on the microstructure for a fixed parameter setting but no significant influence could be detected [26]. The altered chemical composition together with the resulting microstructure also determines the mechanical properties of the built parts. When recycled powder was used instead of virgin powder, a slight increase in Vickers hardness and an increase in tensile strength were observed in some studies [27, 29, 30]. Other recent investigations, however, could not show any significant effects on the mechanical properties [25, 26, 31–33]. A possible explanation for these discrepancies lies in the different chemical compositions of the powder materials used, different degrees of recycling, and generally different process settings. It emerges from this that the influence of the powder properties and their changes through reuse cannot yet be clearly described and therefore require further investigations. In order to be able to describe effects and potential interactions, it is important to carry out investigations for several parameter combinations in accordance with the design of experiments (DoE) approach. This has only been insufficiently considered in previous studies on powder recycling.Besides the oxygen already present within the processed material, the process atmosphere and its residual oxygen content are essential parameters that influence process stability and part quality. Titanium and its alloys are known for their high reactivity and the high temperatures present during laser-based additive manufacturing further facilitate reactions especially with oxygen during processing. Therefore, atmospheric protection must be provided at temperatures over 700 K [8]. Conventionally, the PBF-LB process is conducted under argon shielding gas atmosphere. Yet, residual oxygen contents of around 1000 ppm, which are still present in most machines [34, 35], are sufficient to cause critical oxidations of the processed material since the prevailing oxygen partial pressure is several orders of magnitude above the equilibrium oxygen partial pressure as thermodynamically analyzed by Lee et al. [34]. Small oxidized particles that were affected by the heat diffusing from the melt pool cannot be removed during recycling and can have negative effects on the part properties [36]. While Denti et al. could not observe any sensible oxidation of the built parts [29], a study by Dietrich et al. shows different results. With increasing residual oxygen content within the processing atmosphere, an increasing oxygen content within the built parts and an increase in tensile strength could be observed that the authors attributed to the interstitial effects of oxygen like the impediment of dislocation movement [35]. Furthermore, an earlier work of the authors revealed a significant influence of the residual oxygen content and powder recycling on the roughness and reproducibility [37]. This demonstrates that the residual oxygen content and powder recycling should be considered determining factors for the mechanical properties in PBF-LB/M.

Based on the aforementioned findings, this work focusses on the influence of different processing parameters, including powder reuse and residual oxygen content, on microstructure and mechanical properties. The experiments are planned and statistically evaluated according to the DoE approach. This leads to broader insights and comparability of the parameter influences and their interaction effects.

2 Materials and methods

2.1 Experimental materials

In this study, gas atomized Ti-6Al-4V grade 23 powder supplied by Heraeus Additive Manufacturing GmbH was used. The powder had a specified particle size of 15–53 µm and according to the manufacturer's data sheet the size distribution of the virgin powder exhibits the D-values 22 µm (D10), 38 µm (D50), and 54 µm (D90), measured by air-dispersed laser diffraction according to DIN ISO 13320. These values are the respective percentiles of the cumulative particle size distribution (PSD). To investigate the effect of powder recycling, not only virgin powder was used but also powder that was sieved (mesh size of 63 µm) and reused multiple times. In the employed machine, the powder circulates constantly and is sieved every time before it is supplied in the build chamber. Hence, an exact number of reusing cycles cannot be given.

2.2 Experimental equipment

The experiments were carried out on the industrial machine Lasertec 12 SLM by DMG MORI ADDITIVE GmbH (Bielefeld, Germany). This machine is equipped with a 400-W ytterbium fiber laser (single mode, continuous wave, wavelength 1070 nm) supplying a high-quality laser beam ($M^2 = 1.05$). Experiments were conducted with the

Table 1 Tensile test shape B according to DIN EN ISO 6892-1:2020-06

d_0	L_0	L_c	L_t
5 mm	25 mm	28 mm	80 mm

minimum spot diameter of 35 µm. To prevent oxidation, the machine is flooded with argon. The oxygen content can be set to a specific concentration range that is maintained during processing. If the oxygen content is too high, it is reduced by additional purging with argon. A too low oxygen content is mitigated by leakages of the machine without further intervention. To investigate the influence of the residual oxygen content of the processing atmosphere, two different ranges of oxygen concentrations were implemented, 1150 ppm ± 150 ppm and 2150 ppm ± 150 ppm. Thereby, the oxygen content was monitored by a zirconium dioxide oxygen sensor integrated into the machine.

2.3 Experimental design

For microstructure and hardness investigations, cubes with a side length of 5 mm were built. Tensile test specimens were built in accordance with DIN EN ISO 6892-1:2020-06. They were built with a slightly larger diameter compared to the final geometry and were subsequently machined by turning to eliminate the influence of the rough as-built surface. Test shape B was chosen as a specimen geometry with the parameters given in Table 1.

Table 2 gives an overview over the factors and the levels on which they were varied. The main parameters laser power, scanning speed, and hatch spacing were varied on five levels each that were chosen based on literature [10, 38–40], the machine manufacturer's recommendations, and the authors' experience in this field. For the powder condition, the residual oxygen content and the layer thickness were the only two levels realized, since for every level a new build job is necessary.

The levels of the three main parameters were selected based on the DoE approach and according to a circumscribed central composite design (CCD). This design consists of 8 cube points, 6 star points, and one center point leading to a total of 15 parameter combinations. The applied technique enables the determination of the effects of the varied parameters (factors) on the target sizes (responses), their significance, and possible interaction effects between them. For generation, evaluation, and analysis of the experimental design and data, the statistics software JMP® 15 (SAS Institute Inc.) was used. A significance level of 5 % and equidistant factor levels ($\alpha = 2$, see Table 2) were chosen. Under the condition that there were no significant associated higher order effects, all not significant terms (p-value >0.05) were excluded. Herewith, the principle of strong effect heredity should be followed. The mathematical regression model was fitted using the least squares method. For the cubic specimens, except for the center point, which was repeated 6 times per build job, every experimental point was realized 3 times per build job, which led to a total number of 48 specimens for each build job. The tensile test specimens were manufactured 3 times for each parameter combination including the center point leading to 45 specimens per build job. By varying oxygen content, powder condition, and layer thickness only on two levels, a total number of 8 build jobs was conducted for cubic specimens. For building the tensile test specimens, only the lower residual oxygen content was used and layer thickness and powder condition were varied according to Table 2. This led to 4 conducted build jobs with tensile test specimens. A cross-hatching strategy with a rotation angle of 67° between adjacent layers was applied to realize isotropic properties in horizontal direction. The infill was scanned before the contour and with the same parameters. All specimens were built on Ti-6Al-4V build plates with 3-mm support structures. The tensile test specimens were built upright, so that the build direction was parallel to the testing direction. No preheating of the built plate was applied and the parameter combinations were assigned randomly to the specimen numbers. This way, the influence of recoating direction and shielding gas flow could be minimized. Figure 1 shows the applied build layouts. The same numbers stand for the same parameter combinations in both jobs. Since there were only three center point specimens for the tensile tests, three numbers are missing in this build layout.

Table 2 Levels of the varied processing parameters

Parameter	Levels				
Laser power (W)	115	145	175	205	235
Scanning speed (mm/s)	600	800	1000	1200	1400
Hatch spacing (μm)	40	60	80	100	120
Layer thickness (μm)	30	50			
Residual oxygen content (ppm)*	1150 ± 150**	2150 ± 150			
Powder condition	Virgin	Recycled			

*only varied for cubic specimens; **setting for tensile test specimens

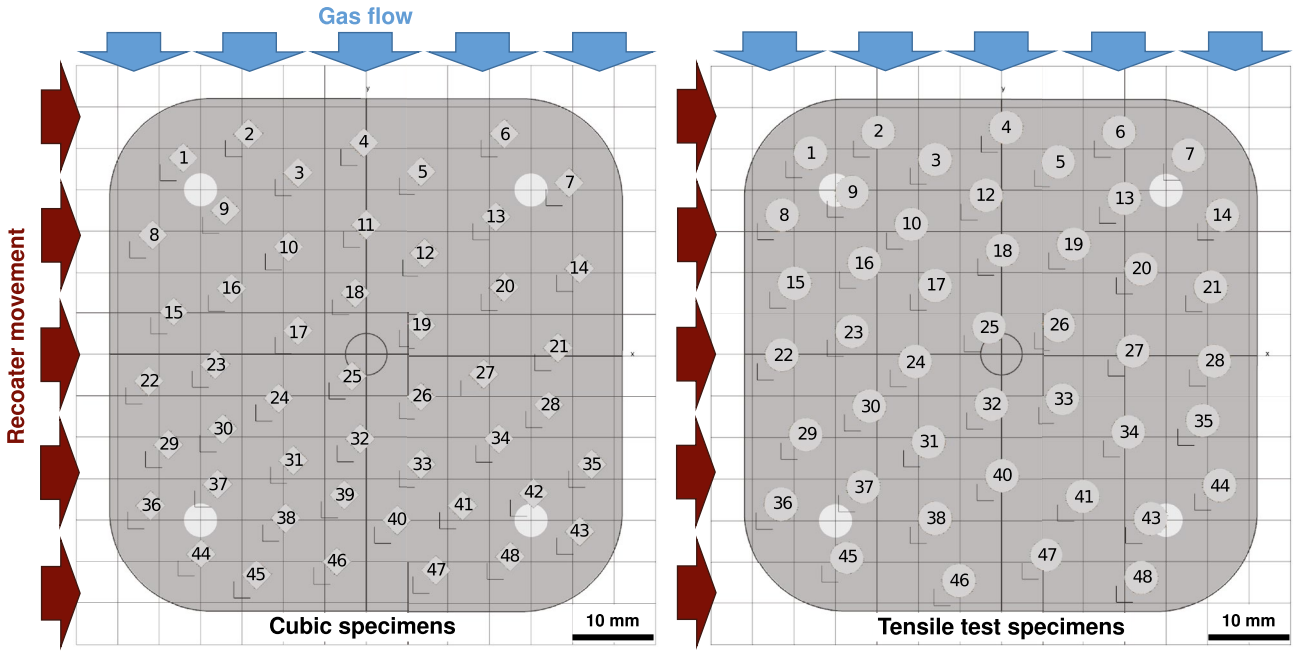

Fig. 1 Build layouts for cubic and tensile test specimens with direction of gas flow and recoater movement

2.4 Methods for analysis

Both types of powder were analyzed using scanning electron microscopy (SEM, Quanta 400 FEG, FEI Company). Based on the SEM images, the particle morphology was examined and the PSD was estimated using the open-source software ImageJ (http://rsb.info.nih.gov/ij/). For analysis of the chemical composition, energy-dispersive X-ray spectroscopy (EDX) measurements were conducted for both powders. The EDX is integrated into the SEM and the analysis was done with the software EDAX Genesis by AMETEK GmbH. Samples of both powders were cold embedded in epoxy resin (Technovit Epox, Kulzer GmbH, Hanau, Germany), ground, and polished (Tegramin, Struers ApS, Ballerup, Denmark). The powder cross-sections were first etched using Kroll's reagent. After microscopic analysis, the cross-sections were polished to remove the etched surface. Afterwards, they were etched again using ammonium bifluoride (ABF) etching, also known as Weck color etching, that is commonly used to make areas with high interstitial oxygen content, such as the α-case, appear bright compared to the remainder of the specimen material. After this etching, the cross-sections were again analyzed using light microscopy. Therefore, the light microscopy functionality of the laser scanning confocal microscope VK-X1000 by Keyence was used. By using different etching methods on the same specimens, it is possible to detect different microstructural features. After processing and removal from the build platform, all cubic specimens were cold embedded, ground, and polished parallel to the build direction (BD), using the same procedure as for the powder samples. Both etching methods were applied to the cross-sections of the cubic specimens. Selected specimens were further examined using X-ray diffraction (XRD, D8 Discover by Bruker with Co Kα radiation) and EDX. After the analysis of the cross-sections, 5 Vickers hardness measurements (INNOVATEST NEXUS 4000 testing machine, HV0.1) with an indentation time of 10 s were conducted for each specimen. The indentations were placed on a line with a distance of 500 µm between each other, starting with a distance of 500 µm to the side surface and ending in the center of the cross-section to be able to detect differences between different specimen areas. The tensile tests were performed according to DIN EN ISO 6892-1:2020-06 with a crosshead speed of 0.42 mm/min equivalent to an initial strain rate of $2.5 \cdot 10^{-4} s^{-1}$. They were conducted at room temperature using a MTS Landmark 100 kN and a MTS axial extensometer with a gauge length of 25 mm. The fracture surface of selected tensile test specimens was analyzed using SEM.

3 Results

3.1 Powder analysis

The SEM images (Fig. 2) revealed mainly spherical particles for both types of powder. The virgin powder shows a significantly higher proportion of fine particles and satellites. For the recycled powder, no satellites could be seen on the SEM images and the particles were of a similar size. Furthermore,

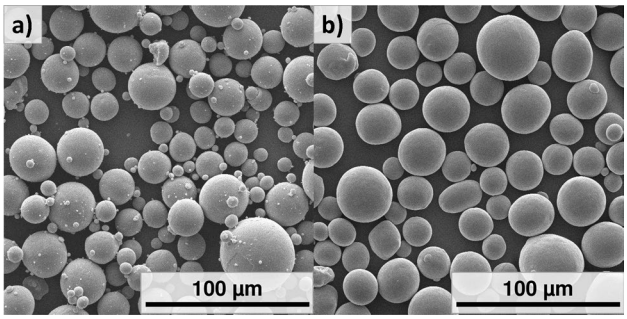

Fig. 2 SEM image of Ti-6Al-4V powder: (**a**) virgin powder, (**b**) recycled powder

the surface appeared smoother than the one of the virgin powder particles.

The analysis of the particle size distribution revealed the *D*-values given in Fig. 3. The PSD of the recycled powder was slightly narrower than the one of the virgin powder and the percentiles (*D*-values) were shifted towards higher values. Additionally, differences between the PSD given by the powder manufacturer for the virgin powder and the PSD calculated in this work could be seen. The values given by the manufacturer were significantly higher.

EDX measurements of the chemical composition allow qualitative comparisons between different material samples. As shown in Table 3, the recycled powder exhibits a higher oxygen content than the virgin powder, while the contents of the alloying elements aluminum and vanadium are comparable.

The etched powder cross-sections (Fig. 4) did not show any significant differences of the microstructure independent of the used etching method. The etching with Kroll's reagent showed a fine martensitic microstructure within the particles. After etching with ABF, the majority of particles

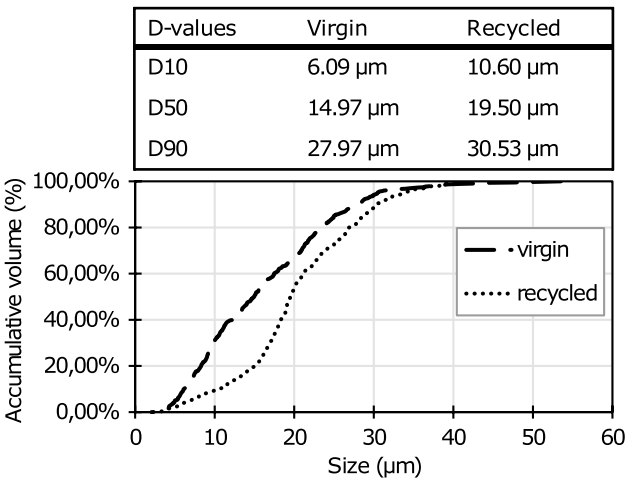

Fig. 3 Particle size distribution of virgin and recycled powder

Table 3 EDX measurements of virgin and recycled powder

Element	Virgin	Recycled
Oxygen (wt%)	5.01	7.38
Aluminum (wt%)	4.30	4.16
Vanadium (wt%)	3.21	3.19
Titanium (wt%)	87.49	85.27

appeared in a dark brown with irregular lighter regions. However, a few particles had a different appearance with a light zone surrounding the darker core. As shown in the image of recycled powder with ABF etching (Fig. 4, lower right), in this light zone a lamellar structure, which becomes coarser towards the surface, could be observed for some particles with this appearance.

3.2 Microstructure

The applied two different etching techniques, Kroll's reagent and ABF etching, provided additional information on different microstructural features. The classical etching with Kroll's reagent makes the elongated prior β-grains and the contained martensite laths visible (Fig. 5). In the center of the specimens, the growth of these grains was mainly parallel to the build direction (BD) while near the surface the growth was rather undirected. The martensitic laths are clearly visible within the prior β-grains with inclination angles of about 45° or –45° towards the build direction for the center section of the specimen. Near the side surface, also larger inclination angles were present at some locations. ABF etching, on the other hand, enables the observation of the layered structure (Fig. 6). At some points (red arrows, Fig. 6), the grain boundaries of the prior β-grains can be recognized since they appear slightly lighter. The visible layers were larger than the applied layer thickness and mainly varied between 50 and 100 µm.

Variations of the microstructure could be observed for varying parameter settings. Figures 7, 8, and 9 juxtapose the two etching results for different cross-sections with increasing laser power, scanning speed, and hatch spacing, respectively. For low laser power (145 W) and high scanning speed (1200 mm/s), a fine-grained structure with thin prior β-grains can be seen. Furthermore, the ABF etching generates a relatively homogeneous brown and bluish appearance of the cross-section. The grain width increases with increasing laser power and decreasing scanning speed up to a point where a high amount of gaseous pores is generated (rightmost cross-section in Fig. 7, leftmost cross-section in Fig. 8). For specimens with a high amount of porosity, a less directed growth of the prior β-grains could be observed. Regarding the influence of the hatch spacing, a significant decrease of the width of prior β-grains could be seen for

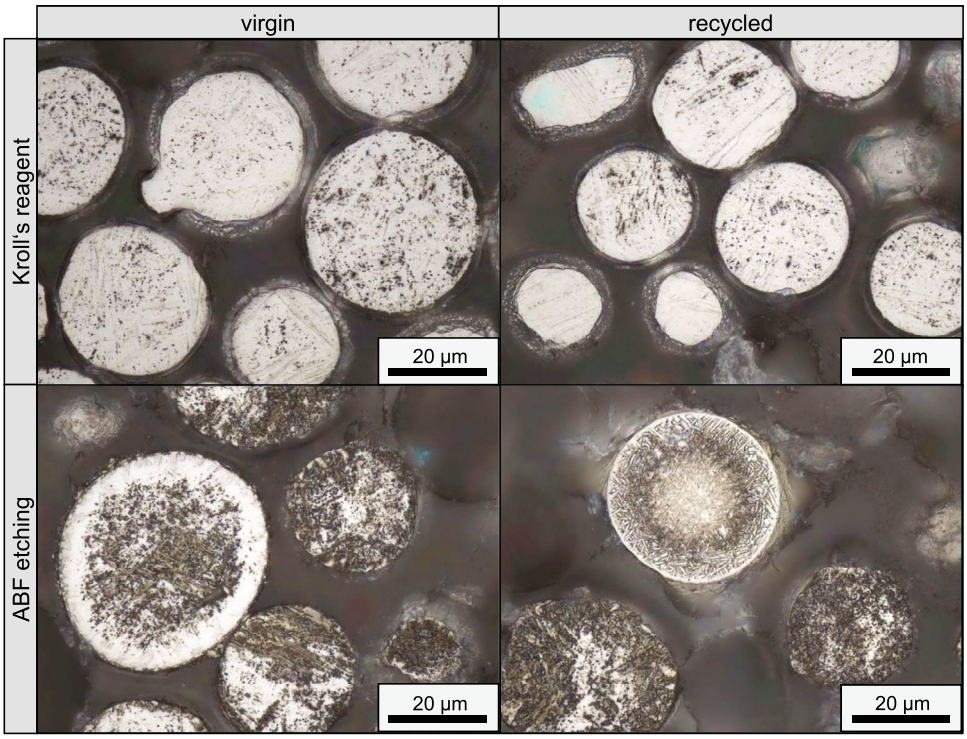

Fig. 4 Cross-sections of virgin and recycled powder, etched with Kroll's reagent and ABF

increasing hatch spacing. At a large hatch spacing (100 µm), the grains were thinner and shorter. Here the ABF etching also generated a homogeneous brown and bluish appearance. With increasing volume energy density, i.e., increasing laser power and decreasing scanning speed and hatch spacing, the layered structure exposed by the ABF etching becomes clearer. It should be emphasized that the top melted layer and regions near the side surfaces are much darker than the rest of the cross-sections. Additionally, alternating lighter and darker horizontal lines are visible. The depth of the dark, top layer and the size of the dark regions at the sides increase with increasing volume energy density. They reach depths of up to several hundred micrometers. While the main processing parameters that were varied according to the CCD experimental design all had a significant influence on the microstructure, no influence could be observed for the applied variations of layer thickness, powder condition, and residual oxygen content within the investigated range. Consequently, the figures only display the results for the virgin powder and low residual oxygen content for simplicity.

To further explore the layered structure exposed by the ABF etching and identify differences between the differently colored zones, XRD and EDX were employed for three specimens that were built with different volume energy densities (28.75 J/mm^3, 58.75 J/mm^3, and 85.42 J/mm^3). The selected specimens were manufactured using virgin powder, 50 µm layer thickness and 2150 ± 150 ppm residual oxygen content. For the specimen with E_V = 28.75 J/mm^3, no distinct dark top layer was visible. Therefore, only the center of this specimen was analyzed. For the other two specimens both, the dark top layer and the center of the specimen were analyzed. The XRD traces (Fig. 10) of all specimens showed the same peaks corresponding to hexagonal distorted α/α'-phase. Only for the center of the specimen

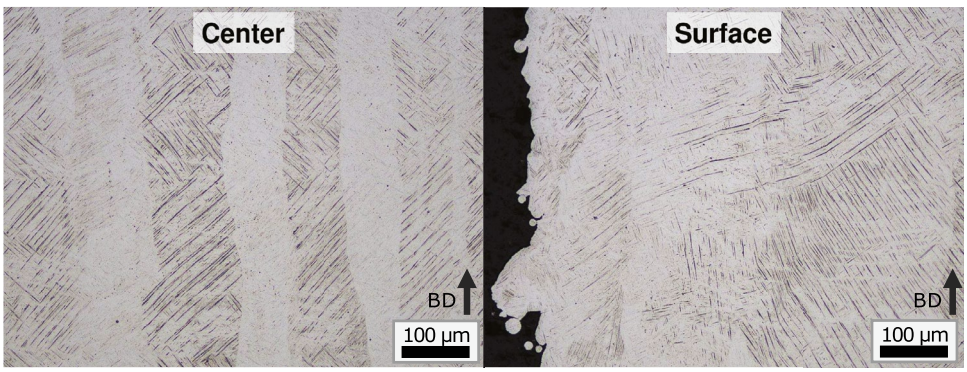

Fig. 5 Center and surface of cross-section etched with Kroll's reagent (center point parameter combination, t = 30 μm, virgin powder, 1150 ± 150 ppm residual oxygen content)

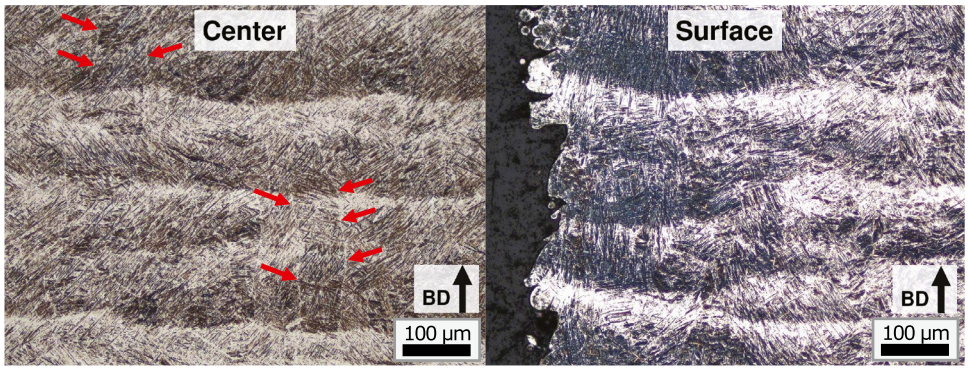

Fig. 6 Center and surface of cross-section etched with ABF (center point parameter combination, $t = 30\ \mu$m, virgin powder, 1150 ± 150 ppm residual oxygen content), β -grain-boundaries indicated by red arrows

with $E_V = 85.42$ J/mm^3 (yellow trace), an additional small peak at approximately 46° indicates the presence of a very small amount of cubic β-phase. Furthermore, the peaks of the sample manufactured with a volume energy density of 58.75 J/mm^3 are more sharp and with a higher intensity than the peaks for the other samples.

For the lowest energy density (28.75 J/mm^3), a significantly higher oxygen content could be seen in the EDX measurements (Table 4) compared to the higher energy densities. This is counterintuitive and can be explained by inaccuracies in the EDX measurements. Additionally, a difference of the elemental composition between the dark top layer and the lighter center of the specimen could be observed. This difference is stronger for the medium energy density of 58.75 J/mm^3 and negligible for the highest energy density of 85.42 J/mm^3. This shows that contrary to expectations, the bright zones are not richer in oxygen than the dark zones. Therefore, the striped appearance of the cross-sections etched with ABF is caused by other microstructural features that will be addressed in the discussion.

3.3 Hardness

Hardness tests were conducted for all specimens and for different locations on each cross-section. A minimum mean hardness of 305.4 HV and a minimum hardness of a single measurement of 99 HV were measured. The maximum mean hardness was 436.4 HV and the maximum hardness of a single measurement was 470 HV. The conducted statistical analysis revealed different influences of the varied parameters. The most influential factor concerning the mean hardness was the residual oxygen content followed by hatch spacing, powder condition, and laser power (Table 5).

An increase of hardness could be observed with increasing oxygen content, with the use of virgin powder, decreasing hatch spacing and increasing laser power. The other

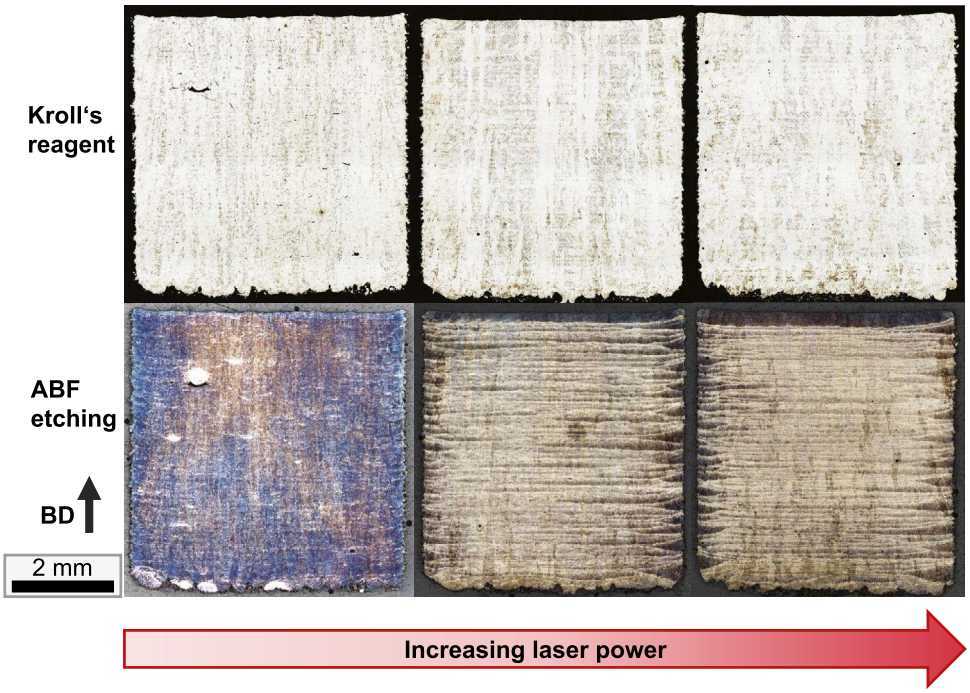

Fig. 7 Cross-sections etched with Kroll's reagent and ABF ($v = 1000$ mm/s, $h = 80\ \mu$m, $t = 30\ \mu$m, virgin powder, 1150 ± 150 ppm residual oxygen content)

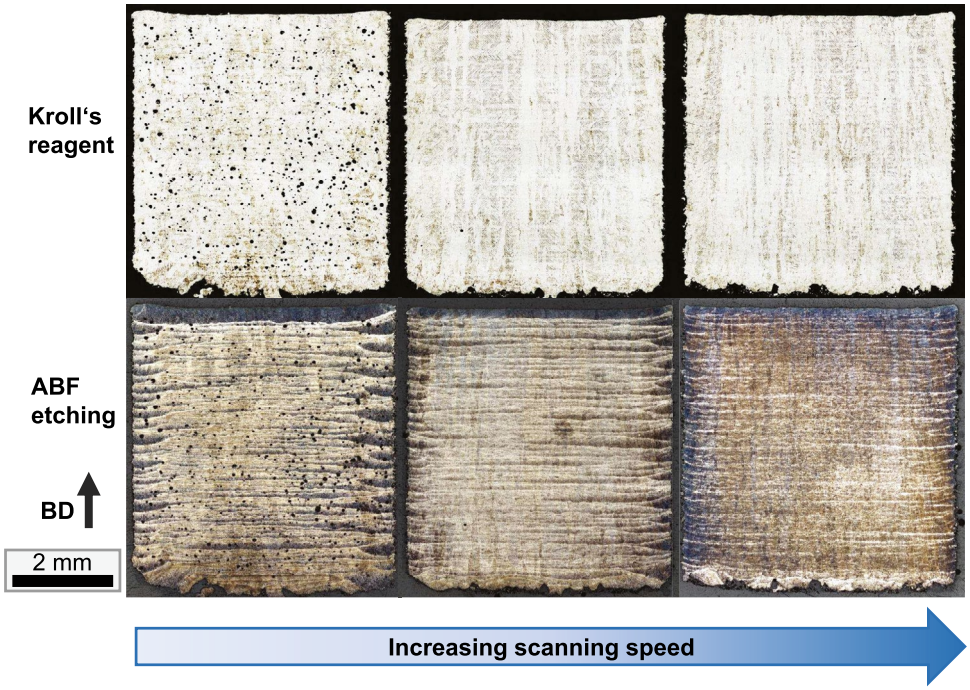

Fig. 8 Cross-sections etched with Kroll's reagent and ABF ($P = 175$ W, $h = 80$ μm, $t = 30$ μm, virgin powder, 1150 ± 150 ppm residual oxygen content)

Fig. 9 Cross-sections etched with Kroll's reagent and ABF ($P = 175$ W, $v = 1000$ mm/s, $t = 30$ μm, virgin powder, 1150 ± 150 ppm residual oxygen content)

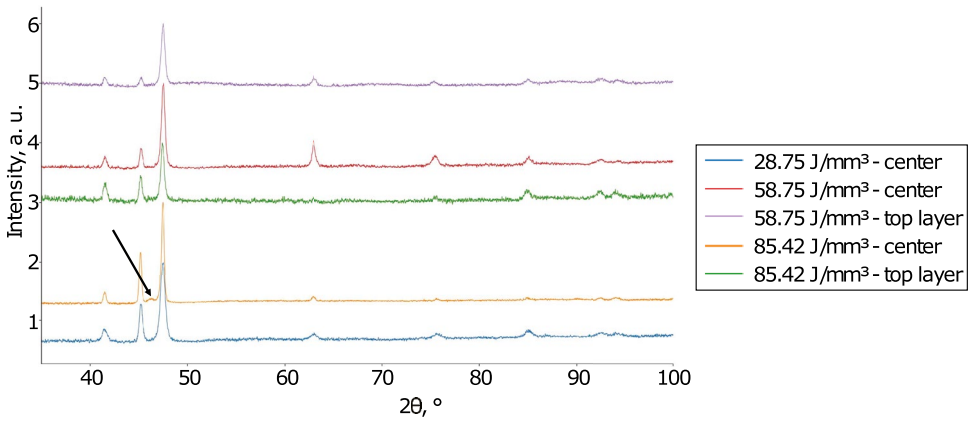

Fig. 10 XRD traces of specimens manufactured with different volume energy densities; the traces have been arranged vertically for clarity; black arrow indicates the peak of cubic β-phase

varied parameters scanning speed and layer thickness also had a significant but smaller influence. The hardness tended to increase with decreasing scanning speed and increasing layer thickness. Figure 11 shows a boxplot graph of the mean hardness in dependence of the four most influential parameters. Table 5 displays the parameter estimates for the fitted model of the mean hardness together with the standard errors, the t-values, and the p-values. The goodness-of-fit for this model is given by $r^2 = 0.53$. Besides the differences regarding the ranking of parameter influences between the hardness at the surface and the one in the center, there is also a difference in the measured hardness value. The hardness is lower near the surface.

3.4 Tensile properties

Within the tensile tests, a mean elastic modulus of 108 GPa was obtained. The maximum ultimate tensile strength (UTS) was 1252.3 MPa (P = 205 W, v = 1200 mm/s, h = 100 µm, t = 50 µm, recycled powder) and the minimum was 703.3 MPa (P = 145 W, v = 800 mm/s, h = 60 µm, t = 50 µm, virgin powder). A maximum elongation at break ϵ of 17.8 % (P = 175 W, v = 1000 mm/s, h = 80 µm, t = 30 µm, virgin powder) and a minimum of 0.8 % (P = 175 W, v = 1000 mm/s, h = 40 µm, t = 50 µm, virgin powder) were observed. Regarding the analysis of effect sizes and significances, the ultimate tensile strength was most influenced by the laser power, followed by hatch spacing and the interaction effect of laser power and scanning speed (Table 6). The powder condition also had a significant influence and recycled powder led to a higher UTS (Table 6). For the maximum elongation in contrast, the powder did not show a significant influence. Here, the laser power was again the most influential factor followed by the scanning speed and the interaction effect of these two factors (Table 7). Since the residual oxygen content was not varied for the tensile test specimens, no statements on this influence can be made. The effects of the three parameters that were varied according to the CCD experimental plan are displayed by the contour plots in Fig. 12. It can be seen that the UTS increased with increasing laser power and increasing hatch spacing, also demonstrated by the signs of the estimates in Table 6. The scanning speed showed a comparably small, antiproportional effect. Similarly, an increase of the elongation is achieved by increasing the laser power and hatch spacing as well as decreasing the scanning speed (Fig. 12; Table 7). Consequently, the UTS correlates with the elongation at break. Brittle specimens with low elongation also tended to fail at comparably low strength. The goodness-of-fit for the regression models is given by $r^2 = 0.74$ and $r^2 = 0.71$ for the UTS and the elongation, respectively.

Selected tensile test specimens were also investigated after failure using SEM. Figure 13 exemplarily displays the SEM images of brittle (a) and ductile (b) fractured surfaces. The brittle fractured surface shows unmelted particles and smooth areas. In contrast, the ductile fractured surface shows a typical dimple structure and visible necking.

Table 4 EDX measurement: elemental composition of specimens manufactured with different volume energy densities E_V

E_V (J/mm^3)	Location	Ti (wt.%)	Al (wt.%)	V (wt.%)	O (wt.%)
28.75	Center	85.88	4.78	3.00	6.34
58.75	Center	88.07	5.12	2.76	4.05
58.75	Surface	87.24	5.04	2.88	4.84
85.42	Center	87.50	4.78	2.94	4.78
85.42	Surface	87.56	4.72	2.87	4.84

4 Discussion

This research focused on the effects of powder recycling and processing atmosphere as well as the conventionally varied processing parameters laser power, scanning speed, hatch spacing, and layer thickness on the microstructure, hardness, and tensile properties. A discussion of the obtained results

Table 5 Parameter estimates of the regression model for the mean hardness

Term	Estimate	Std. error	*t*-value	*p*-value
Intercept	382.1946	2.2423	170.44	< 0.0001
Residual oxygen content [0.13–0.14]	–5.4078	0.5335	–10.14	< 0.0001
Hatch spacing	–4.6464	0.5335	–8.71	< 0.0001
Powder condition [virgin]	4.6349	0.5335	8.69	< 0.0001
Laser power	3.2526	0.5335	6.10	< 0.0001
Scanning speed	–2.4536	0.5335	–4.60	< 0.0001
Scanning speed · Hatch spacing	–2.4490	0.7545	–3.25	0.0013
Residual oxygen content [0.13–0.14] · Powder condition [virgin]	2.3401	0.5335	4.39	< 0.0001
Laser power · Hatch spacing	2.3323	0.7545	3.09	0.0021
Laser power · Scanning speed	1.9344	0.7545	2.56	0.0107
Laser power^2	–1.2722	0.4356	–2.92	0.0037
Residual oxygen content [0.13–0.14] · Hatch spacing	1.2026	0.5335	2.25	0.0248
Residual oxygen content [0.13–0.14] · (Layer thickness–40 μm)	0.2826	0.0533	5.30	< 0.0001
Layer thickness	0.1827	0.0533	3.42	0.0007
Powder condition [virgin] · (Layer thickness–40 μm)	–0.1292	0.0533	–2.42	0.0159

is given in the following subsections. As for all parameter studies, it should be noted that the reproducibility of the results is strongly coupled to the material, equipment, and especially the PBF-LB/M machine system used. Variations in powder properties, laser parameters, or build layouts can lead to different results and parameter effects. Future work will therefore address the transferability of the results between different powders and equipment as well as include confirmatory tests.

4.1 Powder analysis

The powder analysis of the virgin and recycled powder showed differences between the PSD given by the powder manufacturer and the PSD obtained by analysis of SEM images. This can be attributed to the different analysis methods, different powder samples, and different sizes of these samples. Satellite particles that were counted as individual particles in the image analysis might not have been counted using the air dispersed laser diffraction method. Since for that method the sample size is larger, the measurement via diffraction is assumed to be more accurate. Nevertheless, the method using SEM image analysis enables an efficient way of qualitatively comparing different powders. The increase of average particle size and narrowing of the PSD that could be observed was also described in the literature [25, 27, 41]. There are several assumed explanations for this coarsening behavior. During processing, spattering takes place and particle agglomerates as well as melt droplets are formed that can exhibit irregular shapes and larger sizes than the processed powder particles [25, 42, 43]. Other possible reasons could be the size segregation during the

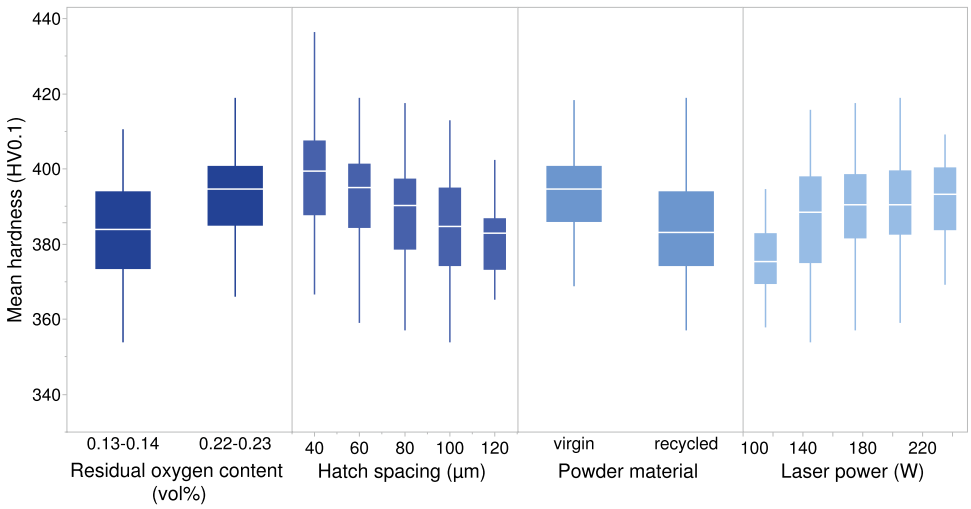

Fig. 11 Boxplot of the mean hardness in dependence of residual oxygen content, powder condition, and hatch spacing

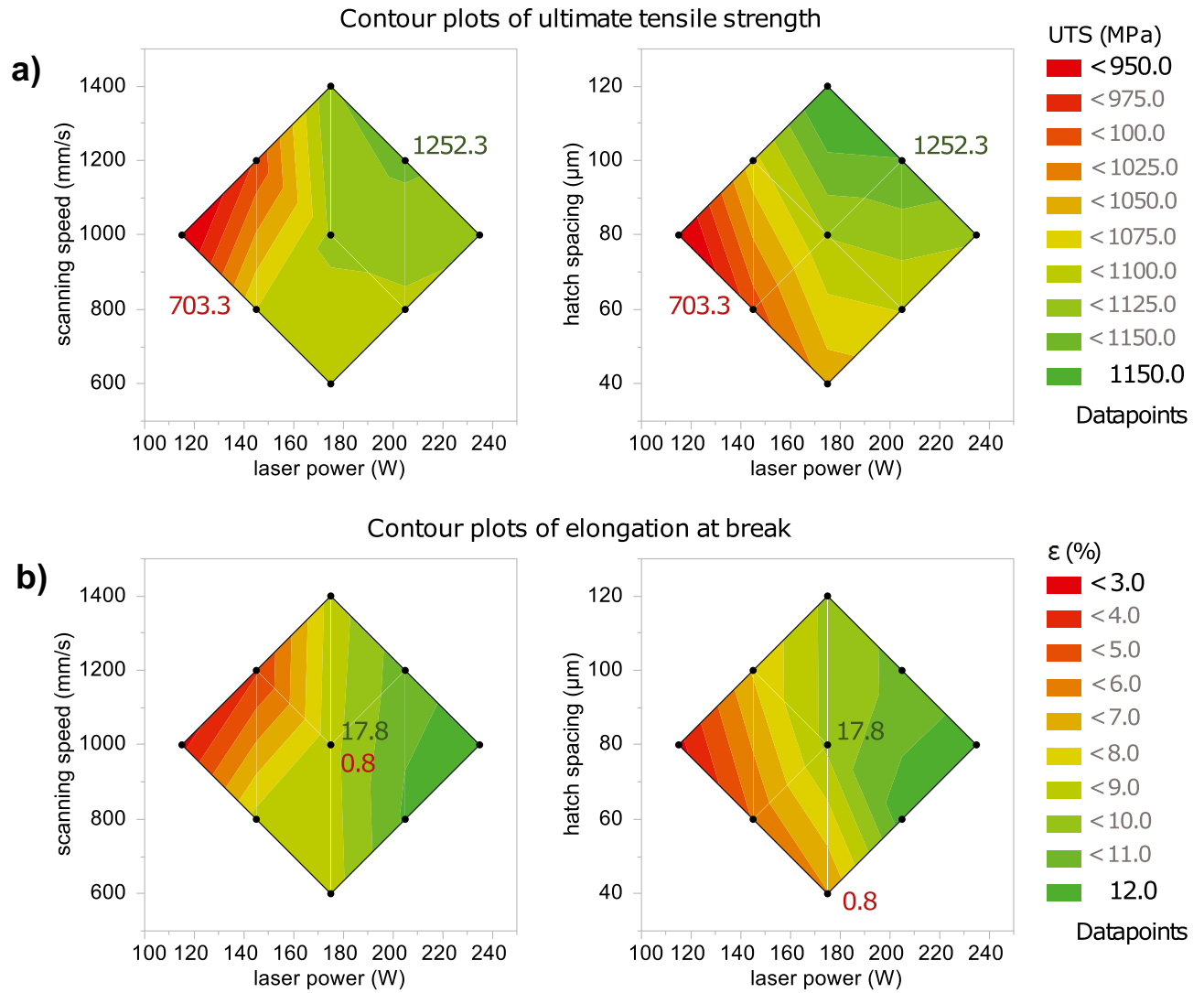

Fig. 12 Contour plot of ultimate tensile strength (**a**) and elongation (**b**) depending on the factors scanning speed, laser power, and hatch spacing; the colors indicate the response values from low (red) to high (green); maximum and minimum values are marked

recoating process or the entrainment of smaller particles by the gas flow [25, 44]. Due to cyclic reheating of the powder around the process zone, oxidation is enhanced which leads to a higher oxygen content in recycled powder. This oxygen contamination at high temperatures is known to cause the so-called α-case, an oxygen-rich layer with stabilized α-phase [9, 45]. By ABF etching, this zone can be made visible for Ti-6Al-4V and some of the powder particles from both powder conditions showed a light outer zone after etching. This indicates that some of the particles experienced a different thermal history resulting in higher oxygen contamination of their surface layer than others. For the recycled powder, these could be particles that were entrained by the gas flow towards the processing zone and which where heated up during interaction with the laser beam. On the other hand, particles with this appearance were also detected for virgin powder indicating that even during powder manufacturing particles experience different thermal histories. However, the etching with Kroll's reagent revealed comparable martensitic microstructures for both types of powder that can be explained by the rapid solidification during powder manufacturing.

4.2 Microstructure

Rapid solidification also takes place during manufacturing of the bulk specimens. It leads to non-equilibrium solidification with the phase transformation $liquid \rightarrow \beta \rightarrow \alpha + \beta/\alpha'$. The β-grains grow parallel to the local conductive heat transfer and in opposite direction of the heat flow, thus towards the

Table 6 Parameter estimates for ultimate tensile strength

Term	Estimate	Std. error	*t*-value	*p*-value
Intercept	1188.0318	18.2839	64.98	< 0.0001
Laser power	45.2968	4.0129	11.29	< 0.0001
Hatch spacing	38.2392	4.0584	9.42	< 0.0001
Laser power · scanning speed	32.9659	5.6749	5.81	< 0.0001
Laser power^2	–24.5831	3.6683	–6.70	< 0.0001
Scanning speed	–23.6187	7.7995	–3.03	0.0029
Powder condition [virgin]	–22.2151	4.1571	–5.34	< 0.0001
Powder condition [virgin] · hatch spacing	10.7347	4.0589	2.64	0.0090
Scanning speed^3	–8.7023	2.6752	3.25	0.0014
Powder condition [virgin] · laser power	8.3073	4.0128	2.07	0.0400
Laser power · (layer thickness—40 μm)	3.1780	0.4013	7.92	< 0.0001
Layer thickness	–2.1805	0.4157	–5.25	< 0.0001
Powder condition [virgin] · (layer thickness—40 µm)	–1.5876	0.4157	–3.82	0.0002
Scanning speed^2	–1.0776	3.6683	–0.29	0.7693
Hatch spacing · (Layer thickness—40 μm)	1.0117	0.4059	2.49	0.0137
Scanning speed · (Layer thickness—40 μm)	–0.8646	0.4013	–2.15	0.0327

melt pool [17]. Metastable acicular α'-martensite forms in the prior β-grains by a diffusionless, shear-type transformation for cooling rates above 10^3 K/s [46, 47]. The martensite needles are oriented about 40° to the building direction (BD) [48] due to the Burgers relation between α/α'-phase and β-phase [49] given in Eqs. (2) and (3).

$$(110)_\beta \leftrightarrow (0001)_\alpha \tag{2}$$

$$\langle 1\bar{1}1\rangle_\beta \leftrightarrow \langle 11\bar{2}0\rangle_\alpha \tag{3}$$

As elucidated by Yang et al. there are four different hierarchical forms of martensite in Ti-6Al-4V manufactured by PBF-LB/M. This hierarchical structure is caused by the cyclic reheating and remelting and some structures can grow over several heating cycles while they limit the growth of smaller structures that form during later cycles [11]. It was also found that the martensite sizes can be influenced by variation of scanning speed and hatch spacing [11], which supports the results of this work. The cyclic reheating also leads to layerwise microstructure coarsening [3] that might lead to the striped appearance of the cross-sections after etching with ABF. Another possible reason for differences in the microstructural appearance in vertical direction are precipitations of intermetallic phases at the bottom of the melt pools as observed by Thijs et al. for increasing energy densities [17]. They also described grain refinement with increasing scanning speed, which is consistent with the results obtained in this work. Our results are further supported by the observations of Kumar et al. and Cepeda-Jiménez et al. stating that a decreasing energy density leads to a decrease of grain width and length. Moreover, incomplete melting

Table 7 Parameter estimates for elongation at break

Term	Estimate	Std. error	*t*-value	*p*-value
Intercept	21.2194	1.0344	20.51	< 0.0001
Laser power	2.2797	0.1912	11.92	< 0.0001
Scanning speed	–1.6807	0.3676	–4.57	< 0.0001
Laser power · scanning speed	1.0000	0.2674	3.74	0.0003
Laser power^2	–0.9610	0.2295	–4.19	< 0.0001
Hatch spacing^2	–0.8472	0.2294	–3.69	0.0003
Laser power · hatch spacing	–0.7958	0.2674	–2.98	0.0034
Scanning speed^2	–0.5992	0.2273	–2.64	0.0092
Hatch spacing	0.4927	0.1912	2.58	0.0108
Scanning speed^3	0.4160	0.1261	3.30	0.0012
Layer thickness	–0.2583	0.0196	–13.15	< 0.0001
Laser power · (layer thickness—40 μm)	0.0671	0.0191	3.51	0.0006
Scanning speed · (layer thickness—40 μm)	–0.0543	0.0189	–2.87	0.0046

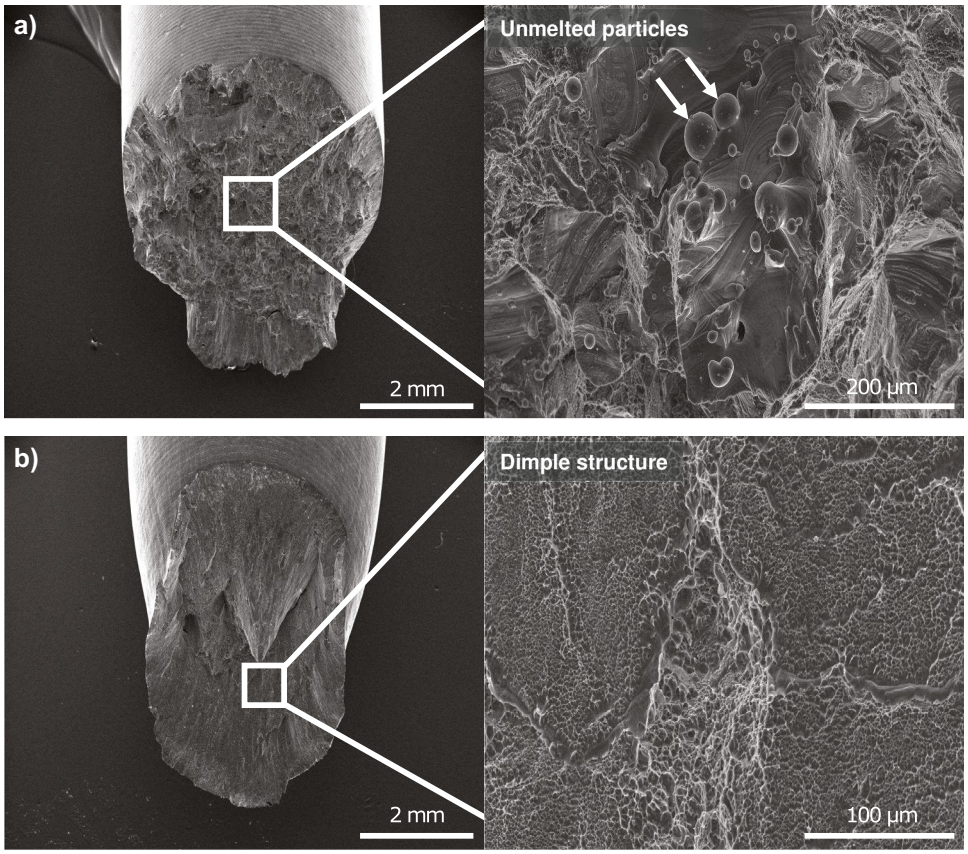

Fig. 13 SEM images of fractured surfaces of tensile test specimens; (**a**) brittle failure (P = 115 W, v = 1000 mm/s, h = 80 μm, t = 30 µm, virgin powder), (**b**) ductile failure (P = 205 W, v = 1200 mm/s, h = 100 µm, t = 30 µm, virgin powder)

causes heterogeneous nucleation sites impeding columnar β-grain growth and therefore causes a fine and weakly textured microstructure [13, 50]. The observed different peak intensities of the XRD spectra can be explained by these differences in microstructure texture as also described by Tseng et al. [51]. Samples with medium volume energy density (e.g., 58.75 J/mm^3) and low porosity showed the strongest texture with vertically aligned prior β-grain and therefore the sharpest XRD peaks. Added to this, the present phases in the as-built state depend on the applied energy density. For a high volume energy density of 85.42 J/mm^3, the XRD also indicated a small amount of the cubic phase besides the hexagonal phase, again with possible effects on the mechanical performance. However, the light microscopic analysis of the etched specimens did not allow for a quantitative evaluation of the different phases. Future research should therefore include further analysis methods like EBSD (electron backscatter diffraction).

4.3 Hardness

The obtained hardness values are comparable with those measured in other studies [13, 17, 52]. In general, additively manufactured parts exhibit higher hardness values in the as-built state compared to conventionally manufactured parts. This is due to the formation of the hard and less ductile α'-martensite phase. Additionally, hardness correlates with residual stresses that are present in the as-built samples and can be reduced by subsequent heat treatments that lead to decomposition of the martensite [53]. As also observed by Thijs et al., a hardness decrease could be seen for increasing scanning speed and hatch spacing [17]. This can be attributed to the bigger surface over which the laser energy is dispersed for a higher hatch spacing and therefore the reduced penetrations depth and remelting of subsequent layers [52]. Scanning with higher speed leads to a lower energy density, thus higher surface tension and impaired wetting which lead to increased porosity and decreased hardness [52]. In contrast to laser power, scanning speed, and hatch spacing, the layer thickness had a weaker effect on the resulting hardness. The hardness tended to increase with increasing layer thickness within the investigated range. This stands in contrast to studies with iron or steel powders, where an increasing layer thickness led to decreasing hardness due to higher porosity [54–56]. However, the layer thickness was only varied on two levels in this work. Consequently, possible effects could not be studied in detail. Besides the processing parameters, the used powder and the residual oxygen content had a significant influence on the hardness with higher hardness for the use of virgin powder and for high residual oxygen

content. A higher oxygen content in the processing atmosphere leads to an increased oxygen uptake of the melt pool. Other than for casted specimens, not only is the surface of a part exposed to a higher oxygen amount. Instead, every layer of the part is exposed to the processing atmosphere so that no α-case can develop. The interstitial oxygen atoms lead to a distortion and tension in the metal lattice and also stabilize the α-phase [45]. This leads to an increase of the hardness. However, near the side surface, the measured hardness was lower than that in the center of the specimens. This can be attributed to different cooling conditions. Near the surface that is surrounded by loose powder, the heat conduction is slower than that in the bulk material. Larger melt pools are formed near the surface and due to slower cooling, less martensite is formed which leads to a decreased hardness. The results concerning the powder condition stand in contrast to other studies. Liu et al. found that a narrower PSD leads to higher hardness while a wider PSD leads to a higher density [57], contradicting the relationship of relative density and hardness described before. Seyda et al. attributed the higher hardness of specimens made of recycled powder to the increased oxygen content [27]. Gorji et al. observed a higher hardness of recycled 316L powder compared to the virgin counterpart and attributed it to the higher porosity of the recycled powder that decreased its hardness [58]. In the present case of higher hardness of the specimens made of virgin powder, this is not a suitable explanation as the porosity was not influenced by the type of powder that was used, as investigated in an earlier work [37]. Consequently, the relationship between the used powder and the resulting hardness seems to be more complex and probably also depends on the alloy itself with its chemical composition and the grade of recycling as well as on the employed experimental equipment. Therefore, confirmatory experiments are needed.

4.4 Tensile properties

The obtained results for UTS and elongation agree well with literature values [3]. The tensile tests revealed a significant influence of the powder condition on the UTS. Since the oxygen content of the recycled powder is higher, it is assumed that the built tensile test samples also contain a higher amount of oxygen. Oxygen is known not only to increase the UTS but also to cause embrittlement [59]. This is due to the impediment of dislocation movement by the oxygen atoms in the metal crystal lattice [60]. An increase in strength of approximately 100 MPa is to be expected for every 0.01 wt% of additional oxygen [61]. However, a significant influence on the elongation could not be observed in this study. Both measures increased with increasing laser power and hatch spacing as well as decreasing scanning speed. Partly, this can be explained by referring to the volume energy density E_V. With increasing E_V, lack of fusion defects that lead to brittle fracture behavior are reduced. Additionally, a higher energy input leads to a decreased cooling rate. Consequently, small amounts of β-phase are able to form and can increase overall ductility. An increasing hatch spacing, however, leads to a decreasing volume energy density. Here, the effect could be explained by the remelting of scan tracks at small hatch spacings. This leads to an increased oxygen pick-up and thus to a more brittle tensile behavior [62]. For further investigation of this correlation, the samples need to be analyzed regarding their oxygen content in future research work.

5 Conclusion

In this work, the influence of different processing parameters including residual oxygen content and powder recycling on the microstructure and mechanical properties was evaluated. The findings can be concluded as follows:

- Powder recycling leads to a larger mean particle size due to the removal of small particles and satellites. Recycled powder has a higher oxygen content.
- The combination of different etching techniques can give additional information on microstructural features. While Kroll's reagent etching highlights the grain structure, ABF etching brings out the layered structure that is attributed to cyclic reheating and coarsening. No significant influence of powder recycling and residual oxygen content on the microstructure was observed. In contrast, the microstructure strongly correlates with the applied volume energy density.
- The hardness was mostly influenced by the residual oxygen content in the processing atmosphere leading to a maximum mean hardness of 436.4 HV0.1. Correlations of the hardness with the other processing parameters are linked to porosity as well as the cooling rate dependent microstructure.
- A maximum ultimate tensile strength of 1252.3 MPa and a maximum elongation of 17.8 % were obtained. While the factor with the strongest influence on the UTS was the used powder condition, the elongation was influenced the most by the layer thickness. Higher elongations can be achieved with a smaller layer thickness. Additionally, a proportional correlation of UTS and elongation at break was observed.

The findings underline the importance to precisely control and minimize the residual oxygen content in the processing atmosphere as well as to take into account the changing powder characteristics during recycling.

Future investigations under oxygen-free atmosphere, central topic of the collaborative research center SFB 1368, therefore promise innovative approaches and new insights. However, the adjustment of the conventionally varied processing parameters in PBF-LB is still key to obtain the desired, reproducible part properties. In general, the results contribute to a better understanding of powder recycling effects and the influence of oxygen and thus to an increase in the sustainability and efficiency of the PBF-LB process.

Acknowledgements The authors would like to thank Khemais Barienti from the Institut für Werkstoffkunde (Materials Science), Leibniz Universität Hannover, for the conduct and analysis of the XRD measurements.

Author contribution Nicole Emminghaus: conception; execute trials; analysis; interpretation; visualization; writing—original draft preparation. Robert Bernhard: writing—review and editing; supervision. Jörg Hermsdorf: writing—review and editing; supervision. Stefan Kaierle: writing—review and editing; supervision

Funding Open Access funding enabled and organized by Projekt DEAL. Funded by the Deutsche Forschungsgemeinschaft (DFG, German Research Foundation) – Project-ID 394563137 – SFB 1368.

Availability of data and material The data is stored in the CKAN repository of the SFB 1368 and is available upon request.

Code availability Not applicable.

Declarations

Conflict of interest The authors declare no competing interests.

References

1. Frazier WE (2014) Metal additive manufacturing: a review. J Mater Eng Perform 23(6):1917–1928. https://doi.org/10.1007/s11665-014-0958-z
2. Gu DD, Meiners W, Wissenbach K, Poprawe R (2012) Laser additive manufacturing of metallic components: Materials, processes and mechanisms. Int Mater Rev 57(3):133–164. https://doi.org/10.1179/1743280411Y.0000000014
3. Liu S, Shin YC (2019) Additive manufacturing of Ti6Al4V alloy: a review. Mater Des 164:107552. https://doi.org/10.1016/j.matdes.2018.107552
4. Singh P, Pungotra H, Kalsi NS (2017) On the characteristics of titanium alloys for the aircraft applications. Mater Today: Proc 4(8):8971–8982. https://doi.org/10.1016/j.matpr.2017.07.249
5. Uhlmann E, Kersting R, Klein TB, Cruz MF, Borille AV (2015) Additive manufacturing of titanium alloy for aircraft components. Procedia CIRP 35:55–60. https://doi.org/10.1016/j.procir.2015.08.061
6. Hao YL, Li SJ, Yang R (2016) Biomedical titanium alloys and their additive manufacturing. Rare Met 35(9):661–671. https://doi.org/10.1007/s12598-016-0793-5
7. Emmelmann C, Scheinemann P, Munsch M, Seyda V (2011) Laser additive manufacturing of modified implant surfaces with osseointegrative characteristics. Phys Procedia 12:375–384. https://doi.org/10.1016/j.phpro.2011.03.048
8. Donachie MJ (2000) Titanium: a technical guide. ASM International
9. Peters M, Leyens C, Kumpfert J (2002) Titan und Titanlegierungen, vol. 2. Wiley-VCH Weinheim
10. Shipley H, McDonnell D, Culleton M, Coull R, Lupoi R, O'Donnell G, Trimble D (2018) Optimisation of process parameters to address fundamental challenges during selective laser melting of Ti-6Al-4V: a review. Int J Mach Tool Manuf 128:1–20. https://doi.org/10.1016/j.ijmachtools.2018.01.003
11. Yang J, Yu H, Yin J, Gao M, Wang Z, Zeng X (2016) Formation and control of martensite in Ti-6Al-4V alloy produced by selective laser melting. Mater Des 108:308–318. https://doi.org/10.1016/j.matdes.2016.06.117
12. Gu D, Hagedorn YC, Meiners W, Meng G, Batista RJS, Wissenbach K, Poprawe R (2012) Densification behavior, microstructure evolution, and wear performance of selective laser melting processed commercially pure titanium. Acta Mater 60(9):3849–3860. https://doi.org/10.1016/j.actamat.2012.04.006
13. Cepeda-Jiménez CM, Potenza F, Magalini E, Luchin V, Molinari A, Pérez-Prado MT (2020) Effect of energy density on the microstructure and texture evolution of Ti-6Al-4V manufactured by laser powder bed fusion. Mater Charact 163:110238. https://doi.org/10.1016/j.matchar.2020.110238
14. Criales LE, Arisoy YM, Lane B, Moylan S, Donmez A, Özel T (2017) Laser powder bed fusion of nickel alloy 625: Experimental investigations of effects of process parameters on melt pool size and shape with spatter analysis. Int J Mach Tool Manuf 121:22–36. https://doi.org/10.1016/j.ijmachtools.2017.03.004
15. Kasperovich G, Haubrich J, Gussone J, Requena G (2016) Correlation between porosity and processing parameters in TiAl6V4 produced by selective laser melting. Mater Des 105:160–170. https://doi.org/10.1016/j.matdes.2016.05.070
16. Carter LN, Wang X, Read N, Khan R, Aristizabal M, Essa K, Attallah MM (2016) Process optimisation of selective laser melting using energy density model for nickel based superalloys. Mater Sci Technol 32(7):657–661
17. Thijs L, Verhaeghe F, Craeghs T, Humbeeck JV, Kruth JP (2010) A study of the microstructural evolution during selective laser melting of Ti-6Al-4V. Acta Mater 58(9):3303–3312. https://doi.org/10.1016/j.actamat.2010.02.004
18. Reisgen U, Olschok S, Sharma R, Gach S (2017) Influence on martensite-start-temperature and volume expansion of low-transformation-temperature materials used for residual stress relief in beam welding. Materialwiss Werkstofftech 48(12):1276–1282. https://doi.org/10.1002/mawe.201700159
19. Welsch G, Boyer R, Collings EW (1993) Materials properties handbook: Titanium alloys. ASM International
20. Santecchia E, Spigarelli S, Cabibbo M (2020) Material reuse in laser powder bed fusion: Side effects of the laser-metal powder interaction. Metals 10(3):341. https://doi.org/10.3390/met10030341
21. Ahmed F, Ali U, Sarker D, Marzbanrad E, Choi K, Mahmoodkhani Y, Toyserkani E (2020) Study of powder recycling and its effect on printed parts during laser powder-bed fusion of 17-4 PH stainless

steel. J Mater Process Technol 278:116522. https://doi.org/10.1016/j.jmatprotec.2019.116522
22. Gunenthiram V, Peyre P, Schneider M, Dal M, Coste F, Fabbro R (2017) Analysis of laser-melt pool-powder bed interaction during the selective laser melting of a stainless steel. J Laser Appl 29(2):022303
23. Scipioni Bertoli U, Guss G, Wu S, Matthews MJ, Schoenung JM (2017) In-situ characterization of laser-powder interaction and cooling rates through high-speed imaging of powder bed fusion additive manufacturing. Mater Des 135:385–396. https://doi.org/10.1016/j.matdes.2017.09.044
24. Matthews MJ, Guss G, Khairallah SA, Rubenchik AM, Depond PJ, King WE (2016) Denudation of metal powder layers in laser powder bed fusion processes. Acta Mater 114:33–42. https://doi.org/10.1016/j.actamat.2016.05.017
25. Sutton AT, Kriewall CS, Karnati S, Leu MC, Newkirk JW (2020) Characterization of AISI 304L stainless steel powder recycled in the laser powder-bed fusion process. Addit Manuf 32:100981. https://doi.org/10.1016/j.addma.2019.100981
26. Carrion PE, Soltani-Tehrani A, Phan N, Shamsaei N (2019) Powder recycling effects on the tensile and fatigue behavior of additively manufactured Ti-6Al-4V parts. JOM 71(3):963–973. https://doi.org/10.1007/s11837-018-3248-7
27. Seyda V, Kaufmann N, Emmelmann C (2012) Investigation of aging processes of Ti-6Al-4V powder material in laser melting. Phys Procedia 39:425–431. https://doi.org/10.1016/j.phpro.2012.10.057
28. Raza A, Pauzon C, Hryha E, Markström A, Forêt P (2021) Spatter oxidation during laser powder bed fusion of Alloy 718: Dependence on oxygen content in the process atmosphere. Addit Manuf 48:102369. https://doi.org/10.1016/j.addma.2021.102369
29. Denti L, Sola A, Defanti S, Sciancalepore C, Bondioli F (2019) Effect of powder recycling in laser-based powder bed fusion of Ti-6Al-4V. Manuf Technol 19(2):190–196. https://doi.org/10.21062/ujep/268.2019/a/1213-2489/mt/19/2/190
30. Quintana OA, Alvarez J, Mcmillan R, Tong W, Tomonto C (2018) Effects of reusing Ti-6Al-4V powder in a selective laser melting additive system operated in an industrial setting. JOM 70(9):1863–1869. https://doi.org/10.1007/s11837-018-3011-0
31. Alamos FJ, Schiltz J, Kozlovsky K, Attardo R, Tomonto C, Pelletiers T, Schmid SR (2020) Effect of powder reuse on mechanical properties of Ti-6Al-4V produced through selective laser melting. Int J Refract Metals Hard Mater 91:105273. https://doi.org/10.1016/j.ijrmhm.2020.105273
32. Alamos FJ, Schiltz J, Attardo R, Aboud Gatrell B, Tomonto C, Budzinski J, McGuffin-Cawley J, Pelletiers T, Schmid SR (2021) Effect of powder reuse on orthopedic metals produced through selective laser sintering. Manuf Lett. https://doi.org/10.1016/j.mfglet.2021.06.002
33. Sun H, Chu X, Liu Z, Gisele A, Zou Y (2021) Selective laser melting of maraging steels using recycled powders: a comprehensive microstructural and mechanical investigation. Metall and Mater Trans A 52(5):1714–1722. https://doi.org/10.1007/s11661-021-06180-1
34. Lee WH, Na TW, Yi KW, Yang SM, Kang JW, Kim HG, Park HK (2020) Thermodynamic analysis of oxidation during selective laser melting of pure titanium. Rapid Prototyp J 26(8):1401–1404. https://doi.org/10.1108/RPJ-08-2019-0226
35. Dietrich K, Diller J, Dubiez-Le Goff S, Bauer D, Forêt P, Witt G (2020) The influence of oxygen on the chemical composition and mechanical properties of Ti-6Al-4V during laser powder bed fusion (L-PBF). Addit Manuf 32:100980. https://doi.org/10.1016/j.addma.2019.100980
36. Williams R, Bilton M, Harrison N, Fox P (2021) The impact of oxidised powder particles on the microstructure and mechanical properties of Ti-6Al-4V processed by laser powder bed fusion. Addit Manuf 46:102181. https://doi.org/10.1016/j.addma.2021.102181
37. Emminghaus N, Hoff C, Hermsdorf J, Kaierle S (2021) Residual oxygen content and powder recycling: Effects on surface roughness and porosity of additively manufactured Ti-6Al-4V. Addit Manuf 46:102093. https://doi.org/10.1016/j.addma.2021.102093
38. Patel S, Vlasea M (2020) Melting modes in laser powder bed fusion. Materialia 9:100591. https://doi.org/10.1016/j.mtla.2020.100591
39. Li Z, Kucukkoc I, Zhang DZ, Liu F (2018) Optimising the process parameters of selective laser melting for the fabrication of Ti6Al4V alloy. Rapid Prototyp J 24(1):150–159. https://doi.org/10.1108/RPJ-03-2016-0045
40. Gorsse S, Hutchinson C, Gouné M, Banerjee R (2017) Additive manufacturing of metals: a brief review of the characteristic microstructures and properties of steels, Ti-6Al-4V and high-entropy alloys. Sci Technol Adv Mater 18(1):584–610. https://doi.org/10.1080/14686996.2017.1361305
41. Ardila LC, Garciandia F, González-Díaz JB, Álvarez P, Echeverria A, Petite MM, Deffley R, Ochoa J (2014) Effect of IN718 recycled powder reuse on properties of parts manufactured by means of selective laser melting. Phys Procedia 56:99–107. https://doi.org/10.1016/j.phpro.2014.08.152
42. Obeidi MA, Mussatto A, Groarke R, Vijayaraghavan RK, Conway A, Rossi Kaschel F, McCarthy E, Clarkin O, O'Connor R, Brabazon D (2020) Comprehensive assessment of spatter material generated during selective laser melting of stainless steel. Mater Today Commun 25:101294. https://doi.org/10.1016/j.mtcomm.2020.101294
43. Ly S, Rubenchik AM, Khairallah SA, Guss G, Matthews MJ (2017) Metal vapor micro-jet controls material redistribution in laser powder bed fusion additive manufacturing. Sci Rep 7(1):4085. https://doi.org/10.1038/s41598-017-04237-z
44. Strondl A, Lyckfeldt O, Brodin H, Ackelid U (2015) Characterization and control of powder properties for additive manufacturing. JOM 67(3):549–554. https://doi.org/10.1007/s11837-015-1304-0
45. Lütjering G, Williams JC (2007) Titanium. Springer Science & Business Media. Google-Books-ID: c9iR1Lm43GEC
46. Oh MS, Lee JY, Park JK (2004) Continuous cooling β-to-a transformation behaviors of extra-pure and commercially pure Ti. Metall Mater Trans A 35(10):3071–3077
47. Ahmed T, Rack HJ (1998) Phase transformations during cooling in a+β titanium alloys. Mater Sci Eng A 243(1):206–211. https://doi.org/10.1016/S0921-5093(97)00802-2
48. Qiu C, Adkins NJE, Attallah MM (2013) Microstructure and tensile properties of selectively laser-melted and of HIPed laser-melted Ti-6Al-4V. Mater Sci Eng A 578:230–239. https://doi.org/10.1016/j.msea.2013.04.099
49. Vrancken B, Thijs L, Kruth JP, Van Humbeeck J (2012) Heat treatment of Ti6Al4V produced by selective laser melting: Microstructure and mechanical properties. J Alloy Compd 541:177–185. https://doi.org/10.1016/j.jallcom.2012.07.022
50. Kumar P, Prakash O, Ramamurty U (2018) Micro-and mesostructures and their influence on mechanical properties of selectively laser melted Ti-6Al-4V. Acta Mater 154:246–260. https://doi.org/10.1016/j.actamat.2018.05.044
51. Tseng JC, Huang WC, Chang W, Jeromin A, Keller TF, Shen J, Chuang AC, Wang CC, Lin BH, Amalia L, Tsou NT, Shih SJ, Huang EW (2020) Deformations of Ti-6Al-4V additive-manufacturing-induced isotropic and anisotropic columnar structures: Insitu measurements and underlying mechanisms. Addit Manuf 35:101322. https://doi.org/10.1016/j.addma.2020.101322

52. Khorasani A, Gibson I, Awan US, Ghaderi A (2019) The effect of SLM process parameters on density, hardness, tensile strength and surface quality of Ti-6Al-4V. Addit Manuf 25:176–186. https://doi.org/10.1016/j.addma.2018.09.002
53. Teixeira S, Silva FJG, Ferreira LP, Atzeni E (2020) A review of heat treatments on improving the quality and residual stresses of the Ti-6Al-4V parts produced by additive manufacturing. Metals 10(8):1006. https://doi.org/10.3390/met10081006
54. Delgado J, Ciurana J, Rodríguez CA (2012) Influence of process parameters on part quality and mechanical properties for DMLS and SLM with iron-based materials. Int J Adv Manuf Technol 60(5–8):601–610
55. Kempen K, Yasa E, Thijs L, Kruth JP, Van Humbeeck J (2011) Microstructure and mechanical properties of selective laser melted 18Ni-300 steel. Phys Procedia 12:255–263. https://doi.org/10.1016/j.phpro.2011.03.033
56. Dingal S, Pradhan TR, Sundar JKS, Choudhury AR, Roy SK (2008) The application of Taguchi's method in the experimental investigation of the laser sintering process. Int J Adv Manuf Technol 38(9):904–914. https://doi.org/10.1007/s00170-007-1154-1
57. Liu B, Wildman R, Tuck C, Ashcroft I, Hague R (2011) Investigation the effect of particle size distribution on processing parameters optimisation in selective laser melting process. Additive Manufacturing Research Group, Loughborough University, pp 227–238
58. Gorji NE, O'Connor R, Brabazon D (2020) X-ray tomography, AFM and nanoindentation measurements for recyclability analysis of 316L powders in 3D printing process. Procedia Manuf 47:1113–1116. https://doi.org/10.1016/j.promfg.2020.04.127
59. Pauzon C, Dietrich K, Forêt P, Dubiez-Le Goff S, Hryha E, Witt G (2021) Control of residual oxygen of the process atmosphere during laser-powder bed fusion processing of Ti-6Al-4V. Addit Manuf 38:101765. https://doi.org/10.1016/j.addma.2020.101765
60. Yu Q, Qi L, Tsuru T, Traylor R, Rugg D, Morris JW, Asta M, Chrzan DC, Minor AM (2015) Origin of dramatic oxygen solute strengthening effect in titanium. Science 347(6222):635–639. https://doi.org/10.1126/science.1260485
61. Barba D, Alabort C, Tang YT, Viscasillas MJ, Reed RC, Alabort E (2020) On the size and orientation effect in additive manufactured Ti-6Al-4V. Mater Des 186:108235. https://doi.org/10.1016/j.matdes.2019.108235
62. Velasco-Castro M, Hernández-Nava E, Figueroa IA, Todd I, Goodall R (2019) The effect of oxygen pickup during selective laser melting on the microstructure and mechanical properties of Ti–6Al–4V lattices. Heliyon 5(12):e02813. https://doi.org/10.1016/j.heliyon.2019.e02813